Review

Recent Progress in Research on Ferromagnetic Rhenium Disulfide

Hongtao Ren [1,*] and Gang Xiang [2,*]

1 School of Materials Science and Engineering, Liaocheng University, Hunan Road No. 1, Liaocheng 252000, China
2 College of Physics, Sichuan University, Wangjiang Road No. 29, Chengdu 610064, China
* Correspondence: renhongtao@lcu.edu.cn (H.R.); gxiang@scu.edu.cn (G.X.)

Abstract: Since long-range magnetic ordering was observed in pristine $Cr_2Ge_2Te_6$ and monolayer $CrCl_3$, two-dimensional (2D) magnetic materials have gradually become an emerging field of interest. However, it is challenging to induce and modulate magnetism in non-magnetic (NM) materials such as rhenium disulfide (ReS_2). Theoretical research shows that defects, doping, strain, particular phase, and domain engineering may facilitate the creation of magnetic ordering in the ReS_2 system. These predictions have, to a large extent, stimulated experimental efforts in the field. Herein, we summarize the recent progress on ferromagnetism (FM) in ReS_2. We compare the proposed methods to introduce and modulate magnetism in ReS_2, some of which have made great experimental breakthroughs. Experimentally, only a few ReS_2 materials exhibit room-temperature long-range ferromagnetic order. In addition, the superexchange interaction may cause weak ferromagnetic coupling between neighboring trimers. We also present a few potential research directions for the future, and we finally conclude that a deep and thorough understanding of the origin of FM with and without strain is very important for the development of basic research and practical applications.

**Keywords:** defects; doping; strain; phase; domain

1. Introduction

In 2017, Zhang et al. [1] and Xu et al. [2] discovered long-range ferromagnetic ordering in both pristine $Cr_2Ge_2Te_6$ and monolayer $CrCl_3$. Two-dimensional ferromagnetism (FM) [3–5] has since then gradually reached an unprecedented level. However, most of the 2D crystals with FM [1–10] have been obtained using mechanical exfoliation, and long-range ferromagnetic order can only be maintained at low temperatures. Instead, the possibility of growing samples of wafer-scale size, and with room temperature ferromagnetism (RTFM), is a prerequisite for the development of spintronic devices. New experimental methods, such as molecular beam epitaxy (MBE) [7,11–13], therefore, have been developed to grow large-scale materials. However, this specific method needs high-vacuum conditions, which limits its wide use. Furthermore, phase engineering [14–17], doping engineering [18–25], strain engineering [4,26–31], as well as light-driven [32,33], gate-tunable [3,34], patterning-induced [35], and sodium- [36,37] or self-intercalated [13,25] and domain engineering [37] have been used to elevate the Curie temperature (T_c). Interestingly, transition metal phosphorus trichalcogenides (MPX_3, where M stands for a transition metal atom and X = S and Se) have also attracted much attention [38,39]. In particular, the pristine MPS_3 exhibited antiferromagnetic (AFM) properties. When the "M" atom is replaced by other transition metal atoms, it may drive the transition from AFM to FM. Despite some progress that has been made, only a few experimental results have reported 2D materials with RTFM [12,27,32,35,36,40].

Inspired by these efforts, many groups have tried to endow intrinsic nonmagnetic materials with magnetism. Unlike other hexagonal (H or 2H) transition metal chalcogenides (TMDs) with high symmetry, the unique distorted (T_d) structure of rhenium disulfide

(ReS$_2$) has a low in-plane symmetry [41], which endows it with strong in-plane anisotropic properties [42–44]. It is worth noting that a series of innovations have also been made in the RTFM of ReS$_2$. For example, Fu et al. [18] discovered in 2018 a ferromagnetic order in an N-doped ReS$_2$ system, which was obtained using a hydrothermal method. More specifically, a phase transition from FM to AFM could be realized by controlling the doping concentration and the doping sites. Furthermore, the mechanically exfoliated and distorted monolayer showed a long-range ferromagnetic order at RT [17,45]. In addition, a biaxial tensile strain was found to enhance the RTFM in the ReS$_2$ web buckles. It is worth mentioning here that the Re-related vacancies play a crucial role for the RTFM of ReS$_2$. Moreover, Loh et al. [37] analyzed parallel mirror twin boundaries (MTBs) in an electrochemical exfoliated ReS$_2$ monolayer by using linearly polarized optical microscopy (OM), angle-resolved polarized Raman spectroscopy (ARPRS), and scanning transmission electron microscopy (STEM). The in-plane biaxial strain in the MTBs was found to enhance the magnetic moment from 0.09 to 1.94 μ_B/supercell. In addition, vacancy defects were created in the ReS$_2$ films using Ar plasma treatments, and the cations were driven into anionic sites by using thermal annealing (to form antisite defects). Interestingly, spin polarization caused by defects can also enhance the occurrence of RTFM.

Here, we will give an overview of the timeline for the occurrence of magnetism in ReS$_2$. As shown in Figure 1, we compare the various strategies for regulating the RTFM, including defect engineering, doping engineering, strain engineering, phase engineering, and domain engineering. Notably, these methods have made large experimental breakthroughs since 2018. However, only a few ReS$_2$ materials have exhibited RTFM. Finally, we will present a few potential research directions for the future. In short, it is very necessary to obtain a deep understanding about the origin of RTFM and strain-tunable RTFM, which will further help the development of spintronics to flourish.
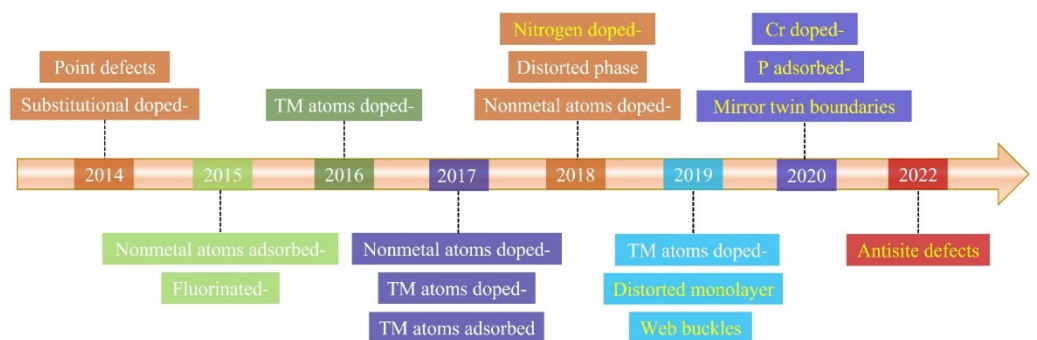

Figure 1. Timeline showing key developments of RTFM in ReS$_2$. White font represents the theoretical progress; yellow font represents the experimental progress.

2. Crystal Structure and Band Structure of ReS$_2$

2.1. Crystal Structure

Monoatomic monolayers such as graphene [44,46,47] have a hexagonal crystal structure (a so-called *H* phase), as shown in Figure 2A. The graphene structure is planar, which is due to the sp^2 hybridization of the carbon atoms. However, the occurrence of sp^3 hybridization causes a buckled structure in, e.g., silicene and germanene.

Like monoatomic crystals, monolayer TMDs consist of three layers of atoms, in which one layer of transition metal (M) atoms is sandwiched by two layers of chalcogeni-de (X) atoms. Chalcogen layers can be stacked on top of each other either as an *H* phase (i.e., with the tetrahedral holes above the transition metal atoms), as in Figure 2A, or as a T_c phase (i.e., with the octahedral holes above the transition metal atoms), as in Figure 2B. There are strong covalent bonds within each layer and weaker van der Waals (vdW) bonds in between. In the octahedral phase, T_c, one of the sulfur layers has been shifted with respect to the other. Notably, ReS$_2$ has a stable distorted octahedral structure, as shown in Figure 2C.
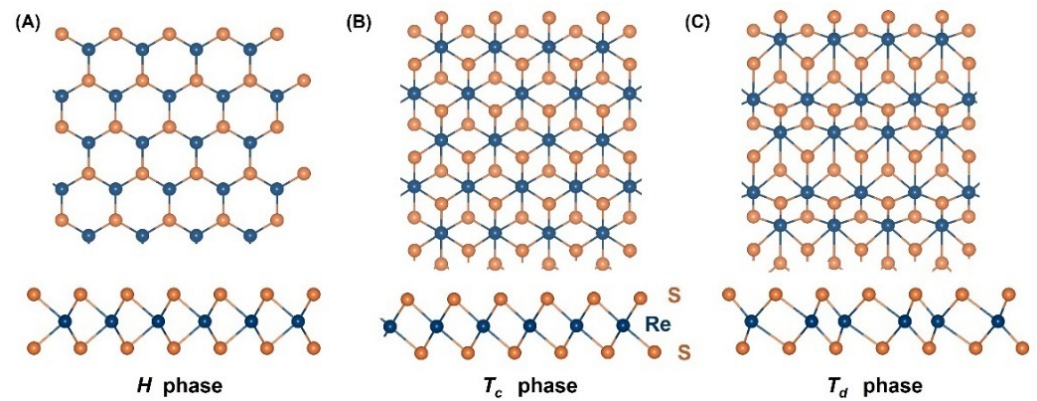
Figure 2. Top and side view of single-layer crystal structures of (**A**) *H* phase, (**B**) T_c phase, and (**C**) T_d phase.

2.2. Band Structure

Bulk ReS_2 is a direct band gap semiconductor with a layered structure, showing novel anisotropic properties [41,48]. As shown in Figure 3A, the crystal structure of ReS_2 with the T_d phase [41] is obviously different from that of MoS_2 with the *H* phase [49,50]. Density functional theory (DFT) calculations show that bulk (1.35 eV) and monolayer (1.43 eV) ReS_2 have similar band structures, both of which are direct band gap semiconductors, but their band gaps are slightly different (only 80 mV difference), as shown in Figure 3B.
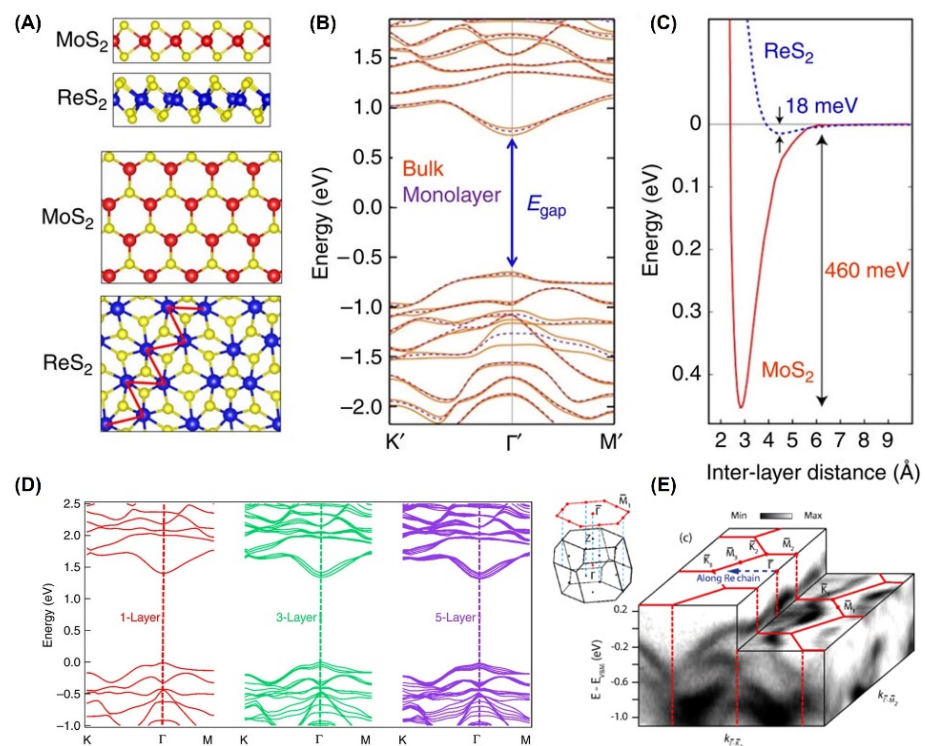
Figure 3. (**A**) Top and side view of single-layer crystal structures of side (top two panels) and top view (bottom two panels) of ReS_2 with T_d crystal structure compared with the 1*H* structure of conventional monolayer TMDs. The Re atoms dimerize as a result of the Peierls distortion forming a Re chain denoted by the red zigzag line. (**B**) DFT calculated electronic band structure of bulk and monolayer ReS_2. Both are predicted to be a direct bandgap semiconductor with nearly identical bandgap value at the Γ point. (**C**) The calculated total energy of the system as a function of interlayer separation. The significantly shallower depth of the well in ReS_2 implies much weaker interlayer coupling energy in

ReS$_2$ as compared with MoS$_2$. (Reprinted figure (**A**–**C**) with permission from [41]. Copyright (2018) by Springer Nature.) (**D**) DFT calculated electronic band structure of monolayer, trilayer, and five-layer ReS$_2$ by ab initio calculations indicating band gaps of 1.44, 1.40, and 1.35 eV, respectively. (Reproduced with permission from [51]. Copyright (2018) by Springer Nature.) (**E**) Overview of the valence-band structure as measured by ARPES, showing strong in-plane anisotropy. The surface Brillouin zone is shown as red lines, and the momentum space direction corresponding to the real-space direction along the Re chains is also indicated. The bulk and projected surface Brillouin zones are shown in the inset. (Reprinted figure with permission from [52]. Copyright (2014) by the American Physical Society).

Actually, the adjacent layers in ReS$_2$ are only weakly coupled (~18 meV) in Figure 3C, whereas those in MoS$_2$ are coupled with much higher energy (~460 meV). Interestingly, when the thickness of ReS$_2$ is reduced down to a single layer [51], its electronic band structure does not exhibit a transition from an indirect to a direct bandgap, which is different from that of MoS$_2$. The bandgap of bulk, trilayer, and monolayer ReS$_2$ are 1.35 eV, 1.40 eV, and 1.44 eV, respectively, as shown in Figure 3D. In experiment, the electrical band structure of rhenium disulfide can be accurately described by angle-resolved photoemission spectroscopy (ARPES) measurements [52]. Although the surface Brillouin zone of ReS$_2$ is almost hexagonal, its electronic structure shows significant in-plane anisotropy, resulting in unique anisotropic optical and electrical properties.

3. Progress in Theoretical Calculations and Experimental Studies of ReS$_2$ Magnetism

3.1. Defect Engineering

Generally, the unintentional generation of defects is unavoidable in the growth, peeling, and transferring of single-layer crystals, which often deteriorates the properties of the materials. Meanwhile, the intentional introduction of defects may induce new properties to the materials. Therefore, defect engineering [53–56] has become an important strategy to use for the modification of material properties. Experimentally, defects are often introduced into the parent materials by means of ion irradiation [57–63], plasma treatment [64], thermal annealing [60,63–67], etc. In 2014, Peter et al. [57] studied the formation energy and stability of lattice defects in monolayer ReS$_2$ by using a combination of experimental and theoretical investigations. The mechanism of defect-mediated magnetism was then revealed. Peeters et al. [49] first introduced point defects in pristine ReS$_2$ by using He ion irradiation. In order to understand the formation energy and stability of these defects, they also carried out first-principle calculations. Optimized atomic structures of a distorted 1T-ReS$_2$ monolayer were then created, as shown in Figure 4. However, the introduction of defects in these optimized structures was not found to change the semiconductor properties or drive any phase transition.

It is worth mentioning that S-related defects (V_S, V_{S+S}, and V_{2S}) cannot cause magnetism, whereas Re-related defects (V_{Re}, V_{ReS} and V_{ReS2}) can. As shown in Figure 5, the magnetization comes predominantly from p orbitals of two neighboring S atoms within the vacancy region.

Interestingly, the antisite defects, such as $S_{S \to Re}$ [57,64] and $S_{2S \to Re}$ [57], bring the magnetic moment of 3 μ$_B$ into the supercell, as shown in Figure 6. However, no RTFM could be detected in the experiments. V_{ReS} and V_{ReS2}, thereafter, can be created by introducing biaxial tensile strain in the ReS$_2$ web buckles (which exist in multiple directions in the plane and cross each other to form some web patterns) [27,68,69].

By performing theoretical calculations, we have also found that V_{Re}, V_{ReS}, and V_{ReS2} can produce a magnetic moment of 1–3 μ$_B$/supercell, as shown in Figure 6A. The supercell size had no obvious effect on the magnetic properties of the system with V_{Re}, V_S, V_{S+S}, V_{2S}, and S_{S-Re}. In contrast, the total magnetic moment of the supercell with V_{ReS} and V_{ReS2} was found to be not only related to supercell size, but also related to the phase. Notably, no matter what type of defects exist, the T_c phase cannot produce a magnetic moment.
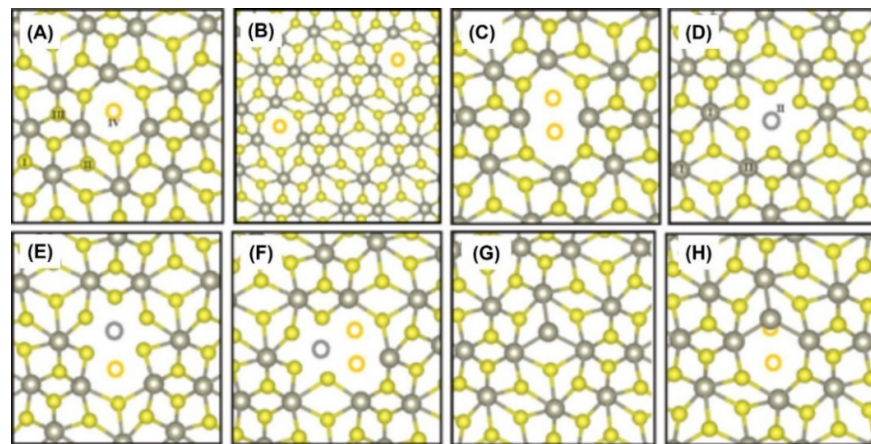
Figure 4. Atomic structure of (**A**) monosulfur vacancy V_S; (**B**) two monosulfur vacancies V_{S+S}; (**C**) disulfur vacancy V_{2S}; (**D**) Re vacancy V_{Re}; (**E**) ReS vacancy V_{ReS}; (**F**) ReS$_2$ vacancy V_{ReS2}; (**G**) single S atom substituted by a Re atom $S_{S \to Re}$; and (**H**) two S atoms substituted by a Re atom $S_{2S \to Re}$. (Reprinted figure with permission from [57]. Copyright (2014) by the American Physical Society.)
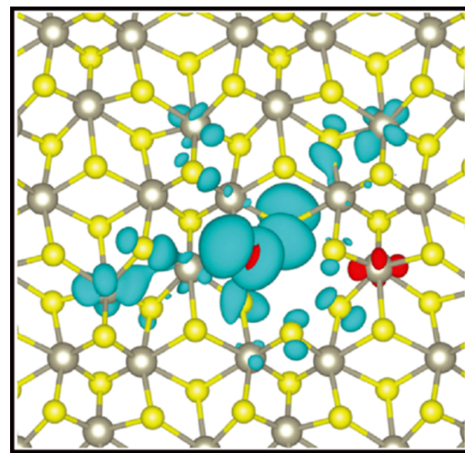
Figure 5. The spin resolved charge density for Re vacancy. Bule (red) colors represent spin up (down) electrons. (Reprinted figure with permission from [57]. Copyright (2014) by the American Physical Society).
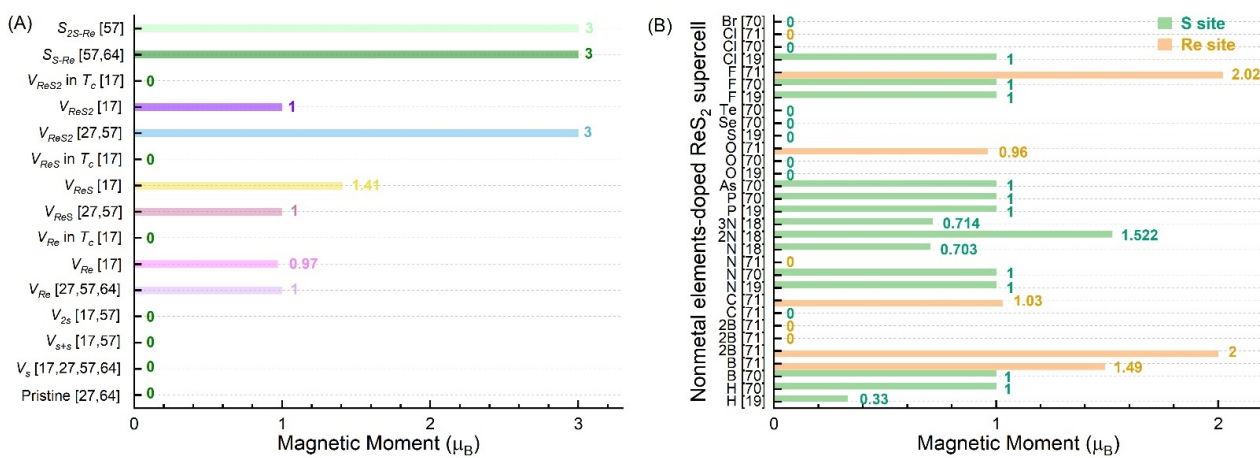
Figure 6. Calculated total magnetic moment in ReS$_2$ supercell with different point defects (**A**) and different nonmetallic elements doped (**B**) [17–19,27,57,64,70,71]; T_d phase: noncentrosymmetric; T_c phase [17]: centrosymmetric metallic.

In 2022, antisite defects (e.g., S_{S-Re}) were introduced into 2D ReS_2 flakes using Ar plasma and thermal annealing treatment [64]. Actually, the defects in ReS_2 nanosheets were formed by the Re atoms occupying the positions of the S atoms, and new V_{Re} defects were simultaneously introduced (Figure 6). With an increase in plasma treatment time, the magnetic moment increased at RT in the experiment. The magnetism was enhanced up to ~20 times after the subsequent thermal annealing. The significant increase in magnetism was mainly due to the introduction of antisite defects. Similarly, antisite defects (e.g., Mo_{S_2} and S_{2Mo}) have also been observed in CVD-grown MoS_2 using STEM [72,73] analysis. Even if the theory predicts that these antisite defects could induce magnetism, no relevant magnetism has been observed in the experiment so far.

3.2. Doping Engineering

Doping engineering has become a common strategy for adjusting the properties of a material. In 2014, Peter et al. studied the effects of substitutional doping [70] by non-metallic and metal atoms on electrical and magnetic properties. The modulation of magnetism in the ReS_2 material was, thereafter, studied theoretically by means of non-metallic element adsorption [19], fluorination [19,21,71], transition-metal doping [74,75], and non-magnetic metal doping [76].

3.2.1. Nonmetallic Element Doped ReS_2

Actually, doping elements, substitutional sites, supercell sizes, and the distances between the adsorbed atoms and S atoms have all shown a large effect on the magnetism of ReS_2 in Figure 6B. More specifically, F and B were shown to have the strongest effect on the magnetic properties, whereas H, N, P, As, F, and Cl had the least effect. On the other hand, S, Se, and Te showed no effect on the magnetic properties.

In 2018, Fu et al. [18] prepared N-doped ReS_2 nanospheres with different doping concentrations by using hydrothermal methods, as shown in Figure 7. Nitrogen doping can drive the phase transition of ReS_2 from nonmagnetic to ferromagnetic.

More specifically, nitrogen doping with different dopant concentrations has been realized by varying the mass ratio of ammonium rhenate (NH_4ReO_4) and thiourea (CH_4N_2S). The magnetic moment did reach a value of 2.1 emu/g at 2K, as shown in Figure 7A. The inset in Figure 7A shows the non-zero coercivity, indicating the presence of a magnetic anisotropy in the ReS_2 sample. A distinct exchange bias caused by FM-AFM coupling were also observed, as shown in Figure 7C–D. However, nitrogen doping failed to induce long-range ferromagnetic ordering in the ReS_2 system at RT.

In order to explain the correlation between the doping concentration and the magnetism for the ReS_2 supercell with the T_d phase, the magnetic moment and charge distribution were calculated using VASP, as shown in Figure 8. The supercells with different doping concentrations had the following magnetic moments: 0.703 μ_B for 1N per supercell, 1.522 μ_B for 2N per supercell, and 0.714 μ_B for 3N per supercell. Surprisingly, only 40% of the magnetic moment came from the Re atoms, and N atoms contributed the other 60% (Figure 8A–C). In addition, the AFM moments mainly stemmed from the 5d orbitals of the Re atoms. Thus, the main contribution of magnetism came from the N atoms, as shown by the electron spin up channel of the Fermi level in Figure 8D. In addition, with an increase in nitrogen content, a strong intermediate gap state appeared close to the Fermi level in Figure 8E–F, which indicated that the electrons could conduct along the Re chain by hopping [18]. In this way, FM and AFM domains were formed, resulting in a strong exchange bias (EB) phenomenon.
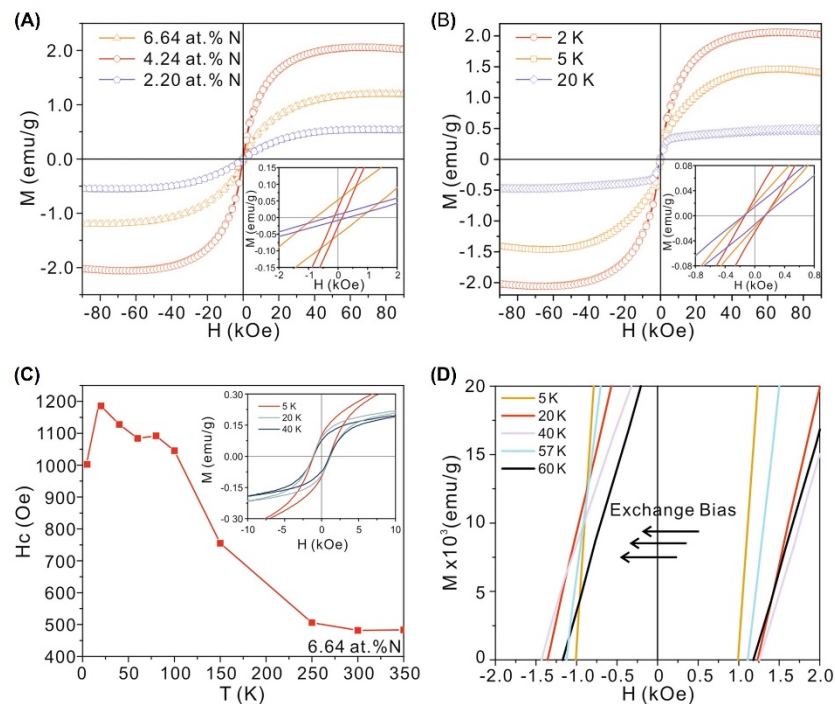
Figure 7. $M-H$ of ReN$_x$ with different nitrogen doping concentrations and detailed analysis with temperature evolution. (**A**) $M-H$ of ReN$_x$ at 2K; the inset shows the non−zero coercivity around the origin. (**B**) $M-H$ of ReN$_{4.24}$ at low temperatures. (**C**) H_c vs T of the ReN$_{6.64}$ sample. The inset shows the exchange bias around the Néel point. (**D**) Magnified view of the $M-H$ of ReN$_{6.64}$. (Reproduced with permission from [18]. Copyright 2018, Springer Nature.)
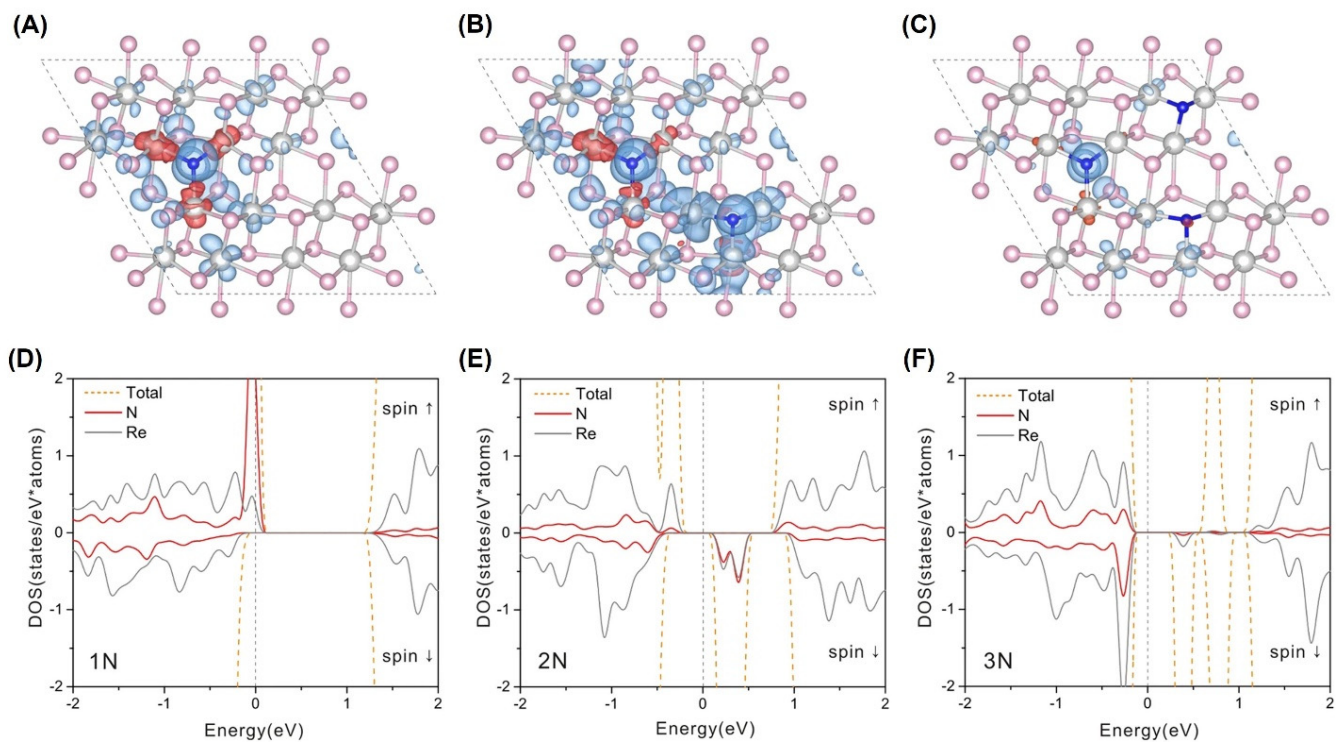
Figure 8. (**A**−**C**) The configuration view of ReN$_x$, with positive (negative) spin densities plotted in blue (red) for isosurfaces at 1×10^{-3} eÅ^{-3}. (**D**−**F**) The corresponding DOS plots of ReS$_2$ doped with 1N, 2N, and 3N, respectively. (Reproduced with permission from [18]. Copyright 2018, Springer Nature).

Notably, Gao et al. [77] realized an intrinsic RTFM by the adsorption of P onto ReS_2 nanosheets. Firstly, ReS_2 powder was synthesized using a hydrothermal method with ammonium rhenate (NH_4ReO_4), hydroxylammonium chloride ($NH_2OH \cdot HCl$), and thiourea (CH_4N_2S) as precursors. Secondly, the obtained powder was placed in a tubular furnace and phosphated with sodium dihydrogen phosphate (NaH_2PO_2) in an Ar atmosphere. Furthermore, the adsorption of different concentrations of phosphorus was realized by varying the treatment time and the dose of NaH_2PO_2. An RTFM as high as 0.0174 emu/g was experimentally obtained, which was caused by the hybridization of Re *d* and P *p* orbitals in the ReS_2 supercell with the T_d phase. The control of the phosphating degree could not only realize the modulation of the magnetic coupling strength, but it could also drive the transformation from AFM to FM. In short, RTFM has been achieved by the adsorption of non-metallic atoms.

Fluorination has often been used as a strategy to mediate the desired properties of materials, as shown in Figure 6B. As early as 2009, Zhou et al. [78] found that graphene can be transformed from metallic to semiconducting, from non-magnetic to magnetic, and from direct band gap to indirect band gap by changing the fluorination degree. In addition, fluorination of boron nitride [79] has been found to increase the structural anisotropy and regulate the spin polarization of the system. Experimentally, graphene samples were fluorinated using the CF_4 radio-frequency plasma technique [80–82] or decomposition of xenon difluoride [83,84] at RT. The observed fluorination-regulated magnetism also initiated a theoretical study of fluorine-modulated 2D magnetism. Different from the degree of fluorination on BN [79], which determines whether the system is FM or AFM, the ground state of F-terminated ReS_2 with T_d phase [21] is AFM. Moreover, its spin configuration depends on the adsorption sites and number of F atoms.

3.2.2. Metal-Doped ReS_2

In 2014, Peter et al. [70] found that it was easier to incorporate metal atoms into the Re sites. After substitutional doping with metal elements such as Li, Na, V, Cu, Nb, Ta, and Ag, as shown in Figure 9A, the ReS_2 supercell with T_d phase was still non-magnetic. No matter whether the dopant was residing on the Re site or the S site, doping with Nb and Ta elements could not introduce magnetism in the ReS_2. However, doping with many other metals, such as Mg, Al, Ti, Cr, Mn, Fe, Co, Zn, Ru, and OS, could introduce magnetism in the ReS_2, as shown in Figure 9B. Interestingly, when Ti, Mn, and Co elements were substitutionally positioned in the S sites, the magnetism disappeared. The bond length between the transition metal atom and the S atom was also found to modulate the magnetic properties [85]. Doping with two metal atoms has also been studied [74,76,85]. It was found that an increased distance between the metal atoms inhibited magnetism.

3.3. Strain Engineering

In 2015, Liu et al. [86] found that a local strain can regulate the optical, electrical, and magnetic properties of single-layer $ReSe_2$ (T_d phase) with band gap energy at 1.15 eV. At first, the mechanically exfoliated $ReSe_2$ nanosheets were deposited on the pre-stretched elastic substrate. The elastic substrate was then released, and straight-edge wrinkles were introduced into the sheet sample. A local strain was introduced into the sample by creating these wrinkles, by which it was possible to modulate the optical band gap and induce magnetism. As shown in Figure 10, the magnetism in the wrinkled zones could be confirmed using magnetic force microscopy (MFM). Liu et al. carried out density functional theory (DFT) calculations to gain more knowledge about the local strain-regulated magnetism. The results showed that the magnetic moment in the flat area was zero, and the magnetic moment in the wrinkled area had increased to a value close to 3.95 μ_B. More specifically, it was found that spin polarization occurred in the wrinkled regions. Furthermore, the effects of uniaxial and biaxial strain on the magnetism were also studied [26]. It was found that compressive strain can annihilate the magnetism of the system and the material can be transformed from half-metal to semiconductor.
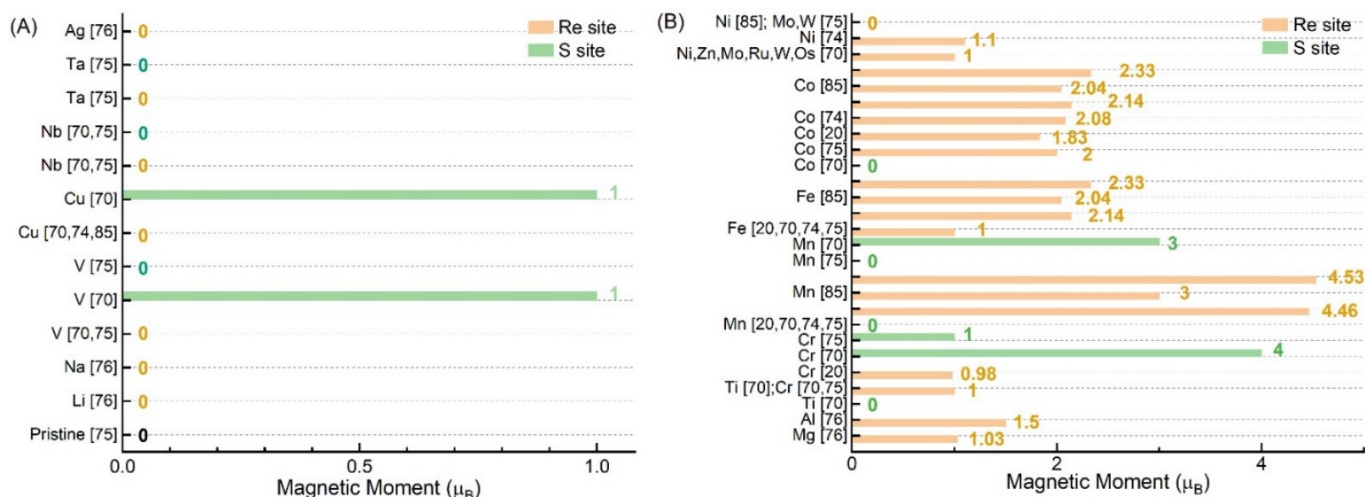
Figure 9. Total magnetic moment of the metal-element doped ReS_2 [20,70,74–76,85]; (**A**) pristine− and doped−ReS_2 supercell at the Re site were still nonmagnetic. (**B**) doped−ReS_2 supercell with one or two atoms exhibited rich magnetic behaviors.
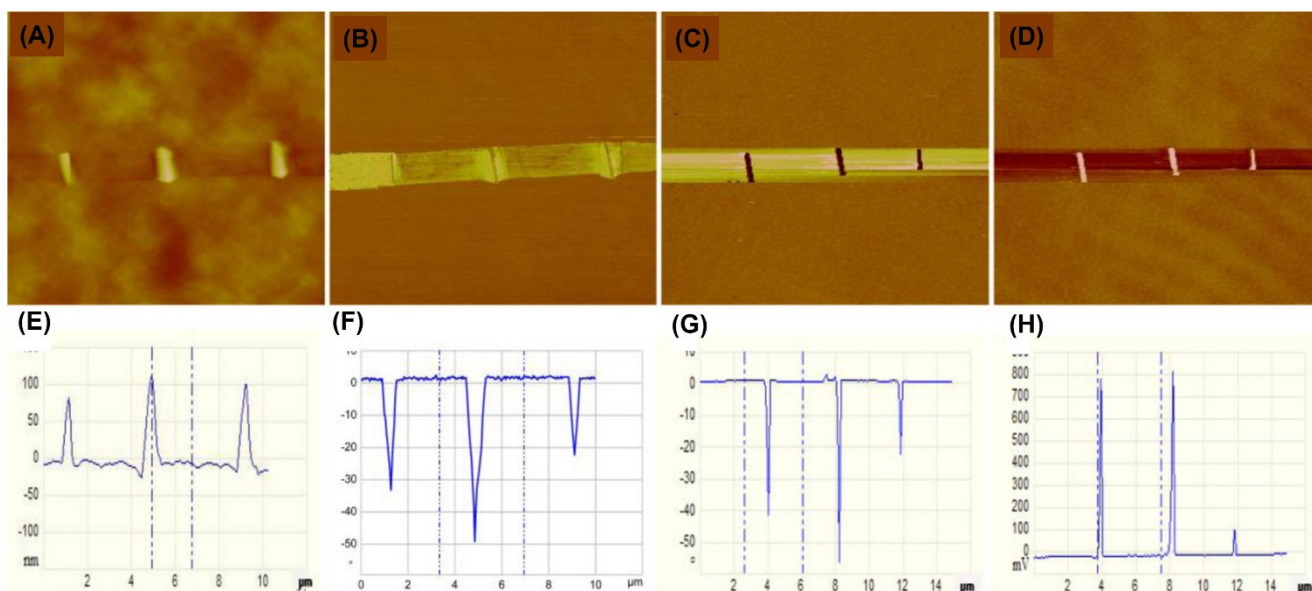
Figure 10. Magnetic force microscopy measurements on $ReSe_2$. (**A**) AFM topography, (**B**) phase, (**C**) MFM phase, and (**D**) MFM amplitude images of monolayer $ReSe_2$ wrinkled flake on gel−film subs−trate. (**E**−**H**) The corresponding profiles in panels (**A**−**D**). Reprinted with permission from [86]. Copyright 2015, American Chemical Society.

However, biaxial strain has never been successfully introduced into Re-based materials, especially in ReS_2. In 2019, we introduced biaxial strain to the film system by spontaneously forming web buckles [27], as shown in Figure 11. As-grown flat ReS_2 films were prepared by polymer-assisted deposition [27,43,63,65–67,69]. Due to the thermal mismatch between the film and the substrate, the compressive biaxial strain was introduced at the bottom of the ReS_2 film.
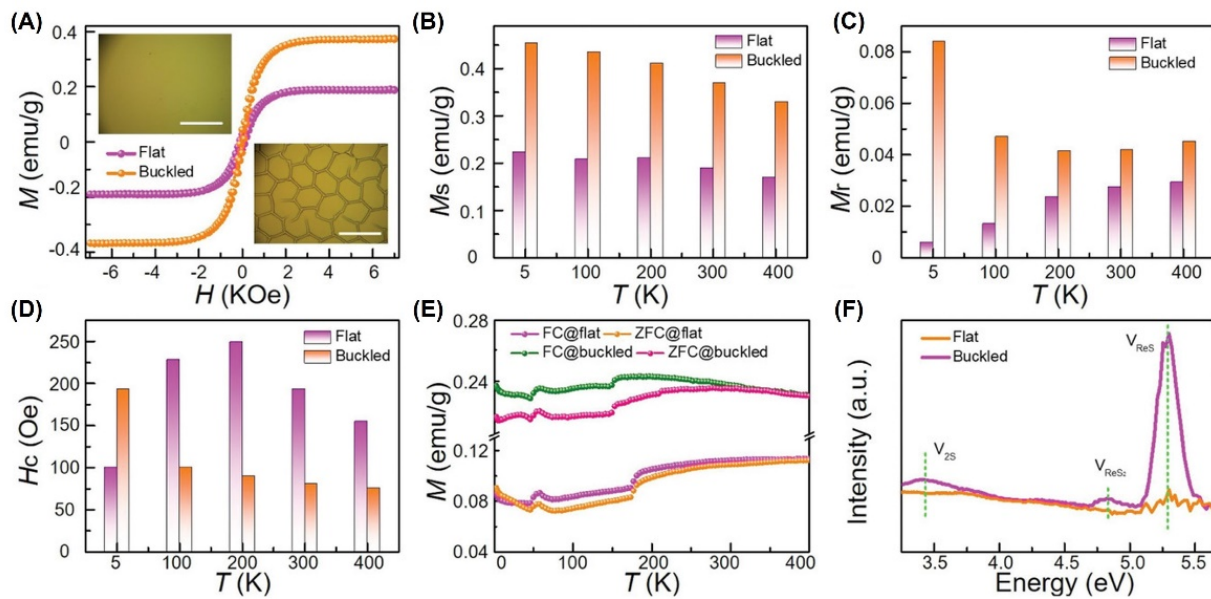
Figure 11. Ferromagnetism of ReS$_2$ thin films. (**A**) M−H curves at 300 K. Scale bar: 50 μm. (**B**−**D**) M_s−T, M_r−T, and H_c−T, respectively. (**E**) FC and ZFC curves from 2 to 400 K. (**F**) FL curves. Reprinted with permission from [27]. Copyright 2019, John Wiley and Sons.

V_{ReS} and V_{ReS2} were created after buckling in Figure 10F. The saturation magnetic moment (M_s) at RT was then found to increase from 0.219 emu/g to 0.370 emu/g, as shown in Figure 11A–B. Similarly, the magnetic moments at other temperatures also increased to various degrees, as shown in Figure 11B. In addition, the residual magnetization (M_r) at 5 K increased by a factor of 14, as shown in in Figure 11C. However, the change in coercivity (H_c) was more complex, showing a nonlinear variation with temperature, as depicted in Figure 11D. Moreover, the Curie temperature (T$_c$) of the material was greater than 400 K. Interestingly, the in-plane magnetic response was weaker than the out-of-plane magnetic response, which was similar to other typical 2D materials.

In order to clarify the origin of RTFM without and with strain, we also carried out spin density calculations using VASP. In fact, the pristine ReS$_2$ crystal with T_d phase was found to be non-magnetic. When Re-related defects were introduced, the system would become magnetic, as shown in in Figure 12A–F. Further, the magnetism clearly changed when a strain was applied to the system. Interestingly, the calculated results showed that the compression strain suppressed the magnetism, and the magnetism became enhanced after a reduction in the compressive strain, as shown in Figure 12G–I. In fact, when the compressive strain decreased from −8% to −5% (V_{Re}), and from −5% (V_{ReS}) to −2% (V_{ReS2}), the system could maintain the maximum magnetic moment of 1 μ$_B$/supercell, 1 μ$_B$/ supercell, and 3 μ$_B$/supercell, respectively. However, the magnetic moment remained unchanged with an increase in the tensile strain. Notably, biaxial tensile strain introduced to the system was found to reduce the formation energy of the defects, create more defects, and increase the stability of the defects [87] after buckling. In summary, Re-related defects are not only the origin of RTFM, but they also play a key role in strain-modulated RTFM.
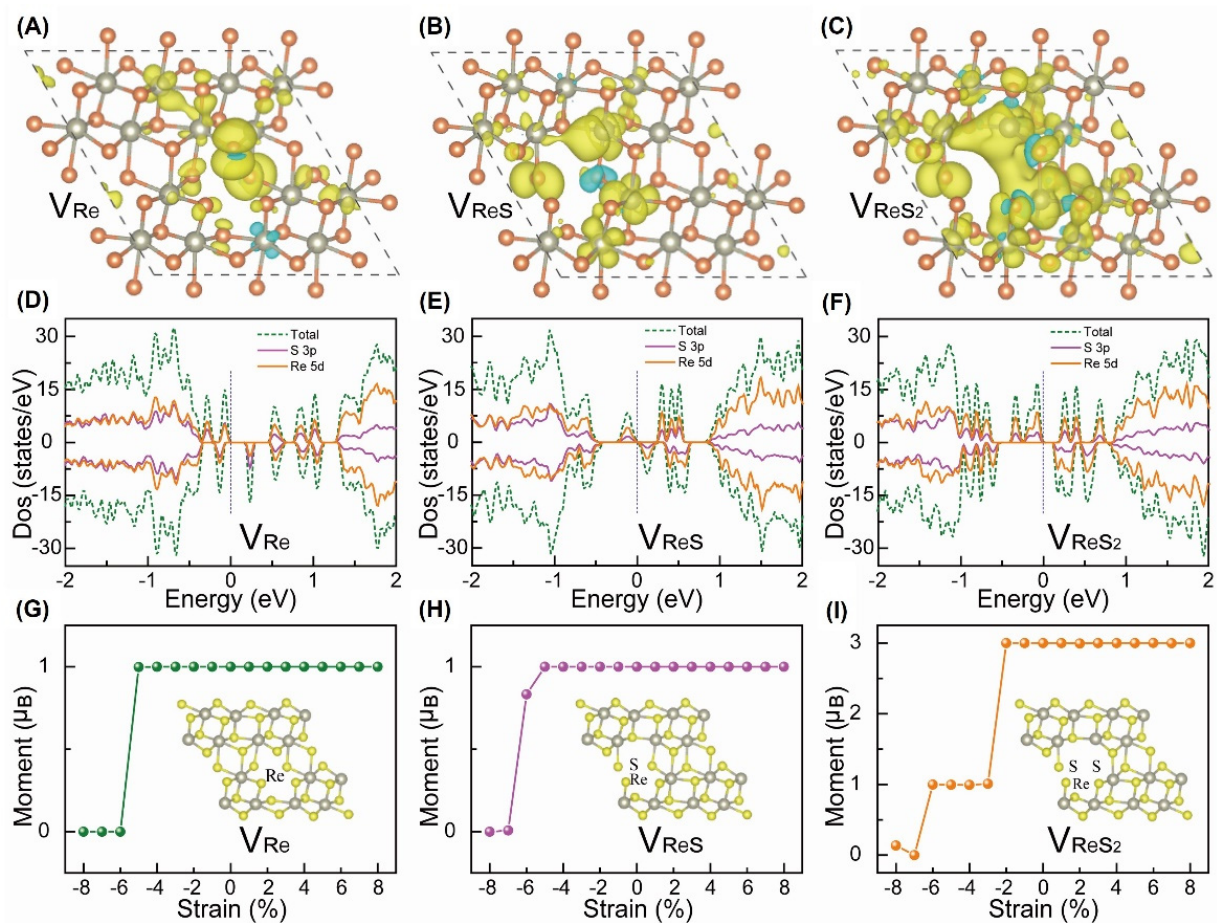
Figure 12. (**A−C**) Magnetic density maps of V_{Re}, V_{ReS}, and V_{ReS2} of ReS$_2$ crystals with up (down) spin densities plotted in yellow (blue) for isosurfaces at 0.001 eÅ^{-3}, respectively. (**D−F**) Orbital projection density of states (PDOS) of V_{Re}, V_{ReS}, and V_{ReS2} of ReS$_2$ crystals, respectively. (**G−I**) The variation in magnetic moment of ReS$_2$ crystal with V_{Re}, V_{ReS}, and V_{ReS2} under biaxial compressive and tensile strain. The inset shows the corresponding crystal structure with vacancy defects. Please note that when the strain value is negative, the strain is compression strain; when the strain is positive, it is a tensile strain. Reprinted with permission from [27]. Copyright 2019, John Wiley and Sons.

3.4. Phase Engineering

ReS$_2$ is a direct band gap semiconductor. ReS$_2$ is usually in the distorted 1*T* phase (T_d phase), which is different from the 2*H* phase of most transition metal chalcogenides. The low symmetry of the structure leads to its diamagnetism. Yang et al. [16] theoretically predicted a new distorted phase (Tri phase) with tunable magnetism. More specifically, the Re atoms formed a uniform-trimer in the second phase. More importantly, the Tri phase could be achieved using doping [20,88] or intercalating [89] of the T_c phase, and it had bipolar magnetic semiconducting behavior (~1.63 eV) at RT. Moreover, it was predicted that carrier doping could not only realize a transformation from a semiconducting phase to a semi-metallic phase, but also raise the T$_c$ to 357K. Furthermore, the overlap of isolated *d* orbitals in the trimer unit forms a direct exchange between *a* (d_{z2}) and e_1 (d_{xy} and d_{x2}) *d* orbitals in Re atoms, which leads to ferromagnetic coupling. Meanwhile, the superexchange interaction between Re *a* and e_1 *d* orbitals is modulated by the 3*p* S orbitals, forming weak ferromagnetic coupling between the neighboring trimers. In short, the direct ferromagnetic coupling between the Re atoms leads to a huge magnetic anisotropy and a high T$_c$. However, the Tri phase has not yet been experimentally obtained.

The migration of out-of-plane electric dipoles was strictly limited by the large potential barrier energy in the T_d phase, which restrained the emergence of ferroelectricity. By

introducing a centrosymmetric metal T_c phase (Figure 2B) into the T_d phase (Figure 2C), a new phase T_t could be constructed, which realized an out-of-plane ferroelectricity, as shown in Figure 13A. When the T_t phase was created by the formation of V_{Re}, a magnetic order in the system was found [17,45,57,90]. Theoretical calculations showed that S atoms at different positions of V_{Re} will cause obvious changes in the magnetism (Figure 13A). Similar to the ReS$_2$ web buckles [27], the out-of-plane FM at RT was about 3.4 times larger than that of the in-plane FM, as shown in Figure 13B. Notably, the mean field approximation showed that T$_c$ could be estimated as 704 K, as shown in Figure 13C–D. The observed FM was found to be very close to V_{Re}.
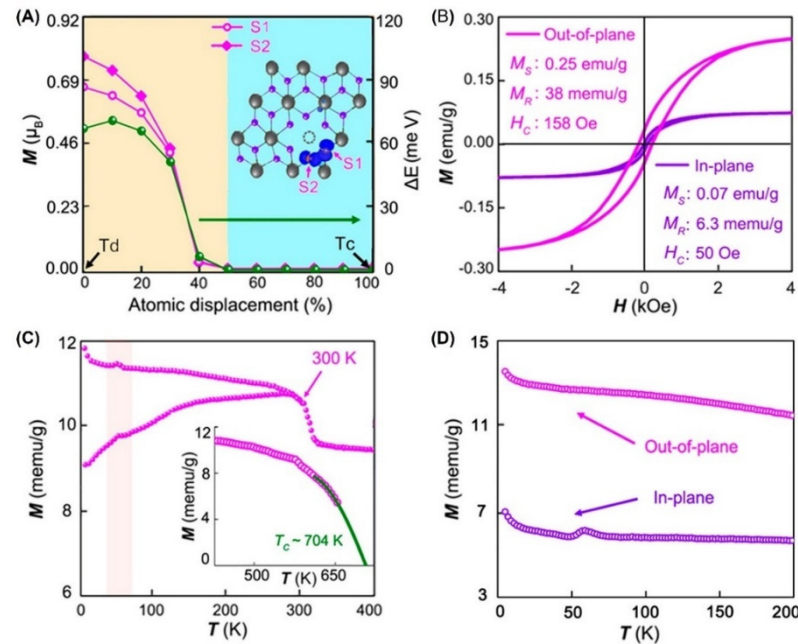
Figure 13. (**A**) Calculated magnetic moment (magenta lines) of atoms S1 and S2 and energy difference between the spin-polarized and spin-unpolarized states (olive line) versus atomic displacement from the T_d to T_c structures (the solid line is a guide for the eye). The inset shows the spin-resolved charge density of the two immediate neighbor atoms S1 and S2 near the Re vacancy (dashed circle). (**B**) Orientation dependence of magnetization at 300 K. (**C**) Temperature dependence of magnetic-field cooling (FC) and zero magnetic-field cooling (ZFC). The extrapolated line at higher temperatures intersects the temperature axis at 704 K, indicating the Curie temperature (inset). (**D**) Temperature dependence of the magnetic susceptibility in the out-of-plane and in-plane directions. Reprinted with permission from [17]. Copyright 2019, American Chemical Society.

3.5. Domain Engineering

A variety of domain structures are often found in MoS$_2$ [91–99], WS$_2$ [100,101] and ReS$_2$ [102] samples that have been prepared by chemical vapor deposition. However, domain engineering is rarely used in exfoliated nanosheets. In 2020, Loh et al. [37] found mirror twin boundaries in pristine ReS$_2$ crystals with the T_d phase using linearly polarized OM, ARPRS, and STEM analysis. Pristine ReS$_2$ crystals were first obtained by electrochemical exfoliation, but FM at low temperatures was observed in intercalated samples. However, spin-polarized calculations showed that the system was non-magnetic whether there were parallel mirror twin boundaries or not. Moreover, the system showed a magnetism after the introduction of sulfur vacancies. The magnetic moment increased from 0.09 μ_B/supercell to 1.94 μ_B/supercell for an applied strain increase of 9%. Interestingly, most of the spins were concentrated on the Re atoms that were close to the grain boundaries. Furthermore, VASP calculations showed that a coexistence lattice strain and V_s at the grain boundaries mainly contributed to FM.

4. Conclusions and Outlook

The construction of a relationship between structure, strain, and magnetism has always been a problem to solve. Although biaxial strain-controlled RTFM has been achieved by buckling, the in-situ variation of RTFM with the buckling process is still unclear. In addition, the influence of uniaxial strain on ferromagnetism has not been clarified, although it is generally believed that a biaxial strain should have a stronger impact on the properties than a uniaxial strain. Therefore, it is of great interest to also explore the effect of a uniaxial strain on the RTFM of ReS_2.

In addition to its potential applications in spintronic materials and devices, ReS_2 has shown promising potentials in other fields. For instance, ReS_2 with a stable T_d phase structure has recently been shown to have potential application possibilities in the fields of photocatalysis [86,103,104], hydrogen evolution reactions (HER) [44,104–109], and lithium-ion batteries [94–103]. This is mainly due to the weak interlayer coupling in ReS_2. Interestingly, an external magnetic field has been used for magnetic catalysts, with the purpose of enhancing the HER and oxygen evolution reaction (OER) activity. Since ReS_2 is a FM material, it has been assumed that ReS_2 can be used as an electrocatalyst. In addition, nanoscale magnetic imaging techniques [110], such as nanowire magnetic force microscopy [111], scanning superconducting quantum interference device microscopy (SQUID) [112], and scanning nitrogen-vacancy center microscopy (SNVM) [113–116], have emerged as important tools in the investigation of 2D materials. These techniques have made it possible to detect magnetism in, e.g., buckled areas. For all the above-mentioned future research directions, a deep understanding of the origin of RTFM and strain-tunable RTFM is necessary, which will further help the development of both basic research and practical applications to flourish.

Author Contributions: Conceptualization, H.R. and G.X.; writing—original draft preparation, H.R.; writing—review and editing, H.R. and G.X.; supervision, G.X. All authors have read and agreed to the published version of the manuscript.

Institutional Review Board Statement: Not applicable.

Informed Consent Statement: Not applicable.

Data Availability Statement: Not applicable.

Conflicts of Interest: The authors declare no conflict of interest.

References

1. Gong, C.; Li, L.; Li, Z.L.; Ji, H.W.; Stern, A.; Xia, Y.; Cao, T.; Bao, W.; Wang, C.Z.; Wang, Y.; et al. Discovery of intrinsic ferromagnetism in two-dimensional van der Waals crystals. *Nature* **2017**, *546*, 265–269. [CrossRef] [PubMed]
2. Huang, B.; Clark, G.; Navarro-Moratalla, E.; Klein, D.R.; Cheng, R.; Seyler, K.L.; Zhong, D.; Schmidgall, E.; McGuire, M.A.; Cobden, D.H.; et al. Layer-dependent ferromagnetism in a van der Waals crystal down to the monolayer limit. *Nature* **2017**, *546*, 270–273. [CrossRef] [PubMed]
3. Gong, C.; Zhang, X. Two-dimensional magnetic crystals and emergent heterostructure devices. *Science* **2019**, *363*, eaav4450. [CrossRef] [PubMed]
4. Miao, F.; Liang, S.-J.; Cheng, B. Straintronics with van der Waals materials. *npj Quantum Mater.* **2021**, *6*, 59. [CrossRef]
5. Zhao, Z.J.; Li, W.; Zeng, Y.; Huang, X.X.; Yun, C.; Zhang, B.; Hou, Y.L. Structure engineering of 2D materials toward magnetism modulation. *Small Struct.* **2021**, *2*, 2100077. [CrossRef]
6. Song, T.C.; Cai, X.H.; Tu Matisse, W.Y.; Zhang, X.O.; Huang, B.; Wilson Nathan, P.; Seyler Kyle, L.; Zhu, L.; Taniguchi, T.; Watanabe, K.; et al. Giant tunneling magnetoresistance in spin-filter van der Waals heterostructures. *Science* **2018**, *360*, 1214–1218. [CrossRef]
7. Liu, S.S.; Yuan, X.; Zou, Y.C.; Sheng, Y.; Huang, C.; Zhang, E.Z.; Ling, J.; Liu, Y.W.; Wang, W.Y.; Zhang, C.; et al. Wafer-scale two-dimensional ferromagnetic Fe_3GeTe_2 thin films grown by molecular beam epitaxy. *Npj 2D Mater. Appl.* **2017**, *1*, 30. [CrossRef]
8. Liu, Y.; Ivanovski, V.N.; Petrovic, C. Critical behavior of the van der Waals bonded ferromagnet $Fe_{3-x}GeTe_2$. *Phys. Rev. B* **2017**, *96*, 144429. [CrossRef]

9. Wang, Y.H.; Xian, C.; Wang, J.; Liu, B.J.; Ling, L.S.; Zhang, L.; Cao, L.; Qu, Z.; Xiong, Y.M. Anisotropic anomalous Hall effect in triangular itinerant ferromagnet Fe_3GeTe_2. *Phys. Rev. B* **2017**, *96*, 134428. [CrossRef]

10. Yi, J.Y.; Zhuang, H.L.; Zou, Q.; Wu, Z.M.; Cao, G.X.; Tang, S.W.; Calder, S.A.; Kent, P.R.C.; Mandrus, D.; Gai, Z. Competing antiferromagnetism in a quasi-2D itinerant ferromagnet: Fe_3GeTe_2. *2D Mater.* **2017**, *4*, 011005. [CrossRef]

11. Roemer, R.; Liu, C.; Zou, K. Robust ferromagnetism in wafer-scale monolayer and multilayer Fe_3GeTe_2. *NPJ 2D Mater. Appl.* **2020**, *4*, 33. [CrossRef]

12. Wang, H.Y.; Liu, Y.J.; Wu, P.C.; Hou, W.J.; Jiang, Y.H.; Li, X.H.; Pandey, C.; Chen, D.D.; Yang, Q.; Wang, H.T.; et al. Above room-temperature ferromagnetism in wafer-scale two-dimensional van der Waals Fe_3GeTe_2 tailored by a topological insulator. *ACS Nano* **2020**, *14*, 10045–10053. [CrossRef] [PubMed]

13. Zhao, X.X.; Song, P.; Wang, C.C.; Riis-Jensen, A.C.; Fu, W.; Deng, Y.; Wan, D.Y.; Kang, L.X.; Ning, S.C.; Dan, J.D.; et al. Engineering covalently bonded 2D layered materials by self-intercalation. *Nature* **2020**, *581*, 171–177. [CrossRef]

14. Cai, L.; He, J.F.; Liu, Q.H.; Yao, T.; Chen, L.; Yan, W.S.; Hu, F.C.; Jiang, Y.; Zhao, Y.D.; Hu, T.D.; et al. Vacancy-induced ferromagnetism of MoS_2 nanosheets. *J. Am. Chem. Soc.* **2015**, *137*, 2622–2627. [CrossRef] [PubMed]

15. Pradhan, N.R.; McCreary, A.; Rhodes, D.; Lu, Z.; Feng, S.; Manousakis, E.; Smirnov, D.; Namburu, R.; Dubey, M.; Hight Walker, A.R.; et al. Metal to insulator quantum-phase transition in few-layered ReS_2. *Nano Lett.* **2015**, *15*, 8377–8384. [CrossRef] [PubMed]

16. Sun, Z.T.; Lv, H.F.; Zhuo, Z.W.; Jalil, A.; Zhang, W.H.; Wu, X.J.; Yang, J.L. A new phase of the two-dimensional ReS_2 sheet with tunable magnetism. *J. Mater. Chem. C* **2018**, *6*, 1248–1254. [CrossRef]

17. Zhang, J.L.; Wu, S.Y.; Shan, Y.; Guo, J.H.; Yan, S.; Xiao, S.Y.; Yang, C.B.; Shen, J.C.; Chen, J.; Liu, L.Z.; et al. Distorted monolayer ReS_2 with low-magnetic-field controlled magnetoelectricity. *ACS Nano* **2019**, *13*, 2334–2340. [CrossRef]

18. Zhang, Q.; Ren, Z.M.; Wu, N.; Wang, W.J.; Gao, Y.J.; Zhang, Q.Q.; Shi, J.; Zhuang, L.; Sun, X.N.; Fu, L. Nitrogen-doping induces tunfable magnetism in ReS_2. *Npj 2d Mater. Appl.* **2018**, *2*, 22. [CrossRef]

19. Zhang, X.O.; Li, Q.F. Electronic and magnetic properties of nonmetal atoms adsorbed ReS_2 monolayers. *J. Appl. Phys.* **2015**, *118*, 064306. [CrossRef]

20. Pan, J.; Zhou, X.Y.; Zhong, J.S.; Hu, J.G. Induction of an atomically thin ferromagnetic semiconductor in 1T' phase ReS_2 by doping with transition metals. *Phys. Lett. A* **2019**, *383*, 125883. [CrossRef]

21. Loh, G.C.; Pandey, R. Robust magnetic domains in fluorinated ReS_2 monolayer. *Phys. Chem. Chem. Phys.* **2015**, *17*, 18843–18853. [CrossRef] [PubMed]

22. Park, S.Y.; Kim, D.S.; Liu, Y.; Hwang, J.; Kim, Y.; Kim, W.; Kim, J.Y.; Petrovic, C.; Hwang, C.; Mo, S.K.; et al. Controlling the magnetic anisotropy of the van der Waals ferromagnet Fe_3GeTe_2 through hole doping. *Nano Lett.* **2020**, *20*, 95–100. [CrossRef] [PubMed]

23. Zhang, S.Z.; Liang, X.; Zhao, H.Y.; Chen, Y.H.; He, Q.; Liu, J.; Lv, L.; Yang, J.H.; Wu, H.L.; Chen, L. Tuning the magnetic properties of Fe_3GeTe_2 by doping with 3d transition-metals. *Phys. Lett. A* **2021**, *396*, 127219. [CrossRef]

24. May, A.F.; Yan, J.Q.; Hermann, R.; Du, M.H.; McGuire, M.A. Tuning the room temperature ferromagnetism in Fe_5GeTe_2 by arsenic substitution. *2D Mater.* **2022**, *9*, 015013. [CrossRef]

25. Mi, M.J.; Zheng, X.W.; Wang, S.L.; Zhou, Y.; Yu, L.X.; Xiao, H.; Song, H.N.; Shen, B.; Li, F.S.; Bai, L.H.; et al. Variation between antiferromagnetism and ferrimagnetism in $NiPS_3$ by electron doping. *Adv. Funct. Mater.* **2022**, *32*, 2112750. [CrossRef]

26. Meng, M.; Shi, C.G.; Li, T.; Shi, S.E.; Li, T.H.; Liu, L.Z. Magnetism induced by cationic defect in monolayer $ReSe_2$ controlled by strain engineering. *Appl. Surf. Sci.* **2017**, *425*, 696–701. [CrossRef]

27. Ren, H.T.; Xiang, G.; Lu, J.T.; Zhang, X.; Zhang, L. Biaxial strain-mediated room temperature ferromagnetism of ReS_2 web buckles. *Adv. Electron. Mater.* **2019**, *5*, 1900814. [CrossRef]

28. Cenker, J.; Sivakumar, S.; Xie, K.C.; Miller, A.; Thijssen, P.; Liu, Z.Y.; Dismukes, A.; Fonseca, J.; Anderson, E.; Zhu, X.Y.; et al. Reversible strain-induced magnetic phase transition in a van der Waals magnet. *Nat. Nanotechnol.* **2022**, *17*, 256–261. [CrossRef]

29. Zhu, M.M.; You, Y.R.; Xu, G.Z.; Tang, J.X.; Gong, Y.Y.; Xu, F. Strain modulation of magnetic coupling in the metallic van der waals magnet Fe_3GeTe_2. *Intermetallics* **2021**, *131*, 107085. [CrossRef]

30. Hu, X.H.; Zhao, Y.H.; Shen, X.D.; Krasheninnikov, A.V.; Chen, Z.F.; Sun, L.T. Enhanced ferromagnetism and tunable magnetism in Fe_3GeTe_2 monolayer by strain engineering. *ACS Appl. Mater. Interfaces* **2020**, *12*, 26367–26373. [CrossRef]

31. Wang, Y.; Wang, C.; Liang, S.J.; Ma, Z.C.; Xu, K.; Liu, X.W.; Zhang, L.L.; Admasu, A.S.; Cheong, S.-W.; Wang, L.Z.; et al. Strain-sensitive magnetization reversal of a van der Waals magnet. *Adv. Mater.* **2020**, *32*, 2004533. [CrossRef] [PubMed]

32. Liu, B.; Liu, S.S.; Yang, L.; Chen, Z.D.; Zhang, E.Z.; Li, Z.H.; Wu, J.; Ruan, X.Z.; Xiu, F.X.; Liu, W.Q.; et al. Light-tunable ferromagnetism in atomically thin Fe_3GeTe_2 driven by femtosecond laser pulse. *Phys. Rev. Lett.* **2020**, *125*, 267205. [CrossRef] [PubMed]

33. Wang, X.; Xiao, C.X.; Park, H.; Zhu, J.Y.; Wang, C.; Taniguchi, T.; Watanabe, K.; Yan, J.Q.; Xiao, D.; Gamelin, D.R.; et al. Light-induced ferromagnetism in moiré superlattices. *Nature* **2022**, *604*, 468–473. [CrossRef] [PubMed]

34. Deng, Y.J.; Yu, Y.J.; Song, Y.C.; Zhang, J.Z.; Wang, N.Z.; Sun, Z.Y.; Yi, Y.F.; Wu, Y.Z.; Wu, S.W.; Zhu, J.Y.; et al. Gate-tunable room-temperature ferromagnetism in two-dimensional Fe_3GeTe_2. *Nature* **2018**, *563*, 94–99. [CrossRef] [PubMed]

35. Li, Q.; Yang, M.M.; Gong, C.; Chopdekar, R.V.; N'Diaye, A.T.; Turner, J.; Chen, G.; Scholl, A.; Shafer, P.; Arenholz, E.; et al. Patterning-induced ferromagnetism of Fe_3GeTe_2 van der Waals materials beyond room temperature. *Nano Lett.* **2018**, *18*, 5974–5980. [CrossRef] [PubMed]

36. Weber, D.; Trout, A.H.; McComb, D.W.; Goldberger, J.E. Decomposition-induced room-temperature magnetism of the Na-intercalated layered ferromagnet $Fe_{3-x}GeTe_2$. *Nano Lett.* **2019**, *19*, 5031–5035. [CrossRef] [PubMed]

37. Yu, W.; Wang, Z.S.; Zhao, X.X.; Wang, J.Y.; Herng, T.S.; Ma, T.; Zhu, Z.Y.; Ding, J.; Eda, G.; Pennycook, S.J.; et al. Domain engineering in ReS_2 by coupling strain during electrochemical exfoliation. *Adv. Funct. Mater.* **2020**, *30*, 2003057. [CrossRef]

38. Autieri, C.; Cuono, G.; Noce, C.; Rybak, M.; Kotur, K.M.; Agrapidis, C.E.; Wohlfeld, K.; Birowska, M. Limited ferromagnetic interactions in monolayers of MPS_3 (M = Mn and Ni). *J. Phys. Chem. C* **2022**, *126*, 6791–6802. [CrossRef]

39. Basnet, R.; Ford, D.; TenBarge, K.; Lochala, J.; Hu, J. Emergence of ferrimagnetism in Li-intercalated $NiPS_3$. *J. Phys. Condens. Mat.* **2022**, *34*, 434002. [CrossRef]

40. Ren, H.T.; Zhang, L.; Xiang, G. Web buckle-mediated room-temperature ferromagnetism in strained MoS_2 thin films. *Appl. Phys. Lett.* **2020**, *116*, 012401. [CrossRef]

41. Tongay, S.; Sahin, H.; Ko, C.; Luce, A.; Fan, W.; Liu, K.; Zhou, J.; Huang, Y.S.; Ho, C.H.; Yan, J.Y.; et al. Monolayer behaviour in bulk ReS_2 due to electronic and vibrational decoupling. *Nat. Commun.* **2014**, *5*, 3252. [CrossRef] [PubMed]

42. Li, X.B.; Dai, X.Y.; Tang, D.Q.; Wang, X.; Hong, J.H.; Chen, C.; Yang, Y.; Lu, J.B.; Zhu, J.G.; Lei, Z.B.; et al. Realizing the intrinsic anisotropic growth of 1T′ ReS_2 on selected Au (101) substrate toward large-scale single crystal fabrication. *Adv. Funct. Mater.* **2021**, *31*, 2102138. [CrossRef]

43. Fadhel, M.M.; Ali, N.; Rashid, H.; Sapiee, N.M.; Hamzah, A.E.; Zan, M.S.D.; Aziz, N.A.; Arsad, N. A Review on rhenium disulfide: Synthesis approaches, optical properties, and applications in Pulsed Lasers. *Nanomaterials* **2021**, *11*, 2367. [CrossRef] [PubMed]

44. Li, X.B.; Chen, C.; Yang, Y.; Lei, Z.B.; Xu, H. 2D Re-based transition metal chalcogenides: Progress, challenges, and opportunities. *Adv. Sci.* **2020**, *7*, 2002320. [CrossRef] [PubMed]

45. Li, L.Z.; Jokisaari, J.R.; Zhang, Y.; Cheng, X.X.; Yan, X.X.; Heikes, C.; Lin, Q.Y.; Gadre, C.; Schlom, D.G.; Chen, L.Q.; et al. Control of domain structures in multiferroic thin films through defect engineering. *Adv. Mater.* **2018**, *30*, 1802737. [CrossRef] [PubMed]

46. Rahman, M.; Davey, K.; Qiao, S.Z. Advent of 2D rhenium disulfide (ReS_2): Fundamentals to applications. *Adv. Funct. Mater.* **2017**, *27*, 1606129. [CrossRef]

47. Yagmurcukardes, M.; Bacaksiz, C.; Unsal, E.; Akbali, B.; Senger, R.T.; Sahin, H. Strain mapping in single-layer two -dimensional crystals via Raman activity. *Phys. Rev. B* **2018**, *97*, 115427. [CrossRef]

48. Wolverson, D.; Crampin, S.; Kazemi, A.S.; Ilie, A.; Bending, S.J. Raman spectra of monolayer, few-layer, and bulk $ReSe_2$: An anisotropic layered semiconductor. *ACS Nano* **2014**, *8*, 11154–11164. [CrossRef]

49. Li, W.B.; Qian, X.F.; Li, J. Phase transitions in 2D materials. *Nat. Rev. Mater.* **2021**, *6*, 829–846. [CrossRef]

50. Voiry, D.; Mohite, A.; Chhowalla, M. Phase engineering of transition metal dichalcogenides. *Chem. Soc. Rev.* **2015**, *44*, 2702–2712. [CrossRef]

51. Liu, E.F.; Fu, Y.J.; Wang, Y.J.; Feng, Y.Q.; Liu, H.M.; Wan, X.G.; Zhou, W.; Wang, B.G.; Shao, L.B.; Ho, C.H.; et al. Integrated digital inverters based on two-dimensional anisotropic ReS_2 field-effect transistors. *Nat. Commun.* **2015**, *6*, 6991. [CrossRef] [PubMed]

52. Biswas, D.; Ganose, A.M.; Yano, R.; Riley, J.M.; Bawden, L.; Clark, O.J.; Feng, J.; Collins-Mcintyre, L.; Sajjad, M.T.; Meevasana, W.; et al. Narrow-band anisotropic electronic structure of ReS_2. *Phys. Rev. B* **2017**, *96*, 085205. [CrossRef]

53. Liang, Q.J.; Zhang, Q.; Zhao, X.X.; Liu, M.Z.; Wee, A.T.S. Defect engineering of two-dimensional transition-metal dichalcogenides: Applications, challenges, and opportunities. *ACS Nano* **2021**, *15*, 2165–2181. [CrossRef] [PubMed]

54. Jiang, J.; Ling, C.Y.; Xu, T.; Wang, W.H.; Niu, X.H.; Zafar, A.; Yan, Z.Z.; Wang, X.M.; You, Y.M.; Sun, L.T.; et al. Defect engineering for modulating the trap states in 2D photoconductors. *Adv. Mater.* **2018**, *30*, 1804332. [CrossRef]

55. Lin, Z.; Carvalho, B.R.; Kahn, E.; Lv, R.T.; Rao, R.; Terrones, H.; Pimenta, M.A.; Terrones, M. Defect engineering of two-dimensional transition metal dichalcogenides. *2D Mater.* **2016**, *3*, 022002. [CrossRef]

56. Lee, J.; Heo, J.; Lim, H.Y.; Seo, J.; Kim, Y.; Kim, J.; Kim, U.; Choi, Y.; Kim, S.H.; Yoon, Y.J.; et al. Defect-induced in situ atomic doping in transition metal dichalcogenides via liquid-phase synthesis toward efficient electrochemical activity. *ACS Nano* **2020**, *14*, 17114–17124. [CrossRef]

57. Horzum, S.; Cakir, D.; Suh, J.; Tongay, S.; Huang, Y.S.; Ho, C.H.; Wu, J.; Sahin, H.; Peeters, F.M. Formation and stability of point defects in monolayer rhenium disulfide. *Phys. Rev. B* **2014**, *89*, 155433. [CrossRef]

58. Mathew, S.; Gopinadhan, K.; Chan, T.K.; Yu, X.J.; Zhan, D.; Cao, L.; Rusydi, A.; Breese, M.B.H.; Dhar, S.; Shen, Z.X.; et al. Magnetism in MoS_2 induced by proton irradiation. *Appl. Phys. Lett.* **2012**, *101*, 102103. [CrossRef]

59. Komsa, H.-P.; Kotakoski, J.; Kurasch, S.; Lehtinen, O.; Kaiser, U.; Krasheninnikov, A.V. Two-dimensional transition metal dichalcogenides under electron irradiation: Defect production and doping. *Phys. Rev. Lett.* **2012**, *109*, 035503. [CrossRef]

60. Han, S.W.; Hwang, Y.H.; Kim, S.H.; Yun, W.S.; Lee, J.D.; Park, M.G.; Ryu, S.; Park, J.S.; Yoo, D.H.; Yoon, S.P.; et al. Controlling ferromagnetic easy axis in a layered MoS_2 single crystal. *Phys. Rev. Lett.* **2013**, *110*, 247201. [CrossRef]

61. Han, S.W.; Park, Y.; Hwang, Y.H.; Lee, W.G.; Hong, S.C. Investigation of electron irradiation-induced magnetism in layered MoS_2 single crystals. *Appl. Phys. Lett.* **2016**, *109*, 252403. [CrossRef]

62. Rani, R.; Dimple; Jena, N.; Kundu, A.; Sarkar, A.D.; Hazra, K.S. Controlled formation of nanostructures on MoS_2 layers by focused laser irradiation. *Appl. Phys. Lett.* **2017**, *110*, 083101. [CrossRef]

63. Ren, H.T.; Xiang, G. Morphology-dependent room-temperature ferromagnetism in undoped ZnO nanostructures. *Nanomaterials* **2021**, *11*, 3199. [CrossRef] [PubMed]

64. Wu, S.Y.; Yao, J.L.; Gao, J.; Shan, Y.; Liu, L.Z. The exchange between anions and cations induced by coupled plasma and thermal annealing treatment for room-temperature ferromagnetism. *Phys. Chem. Chem. Phys.* **2022**, *24*, 7001–7006. [CrossRef]

65. Ren, H.T.; Xiang, G.; Gu, G.X.; Zhang, X. Enhancement of ferromagnetism of ZnO:Co nanocrystals by post-annealing treatment: The role of oxygen interstitials and zinc vacancies. *Mater. Lett.* **2014**, *122*, 256–260. [CrossRef]

66. Ren, H.T.; Xiang, G.; Gu, G.X.; Zhang, X.; Wang, W.J.; Zhang, P.; Wang, B.Y.; Cao, X.Z. Zinc vacancy-induced room- temperature ferromagnetism in undoped ZnO thin films. *J. Nanomater.* **2012**, *2012*, 295358. [CrossRef]

67. Ren, H.T.; Xiang, G.; Luo, J.; Yang, D.L.; Zhang, X. Direct catalyst-free self-assembly of large area of horizontal ferromagnetic ZnO nanowire arrays. *Mater. Lett.* **2019**, *234*, 384–387. [CrossRef]

68. Wang, E.Z.; Chen, Z.K.; Shi, R.; Xiong, Z.X.; Xin, Z.Q.; Wang, B.L.; Guo, J.; Peng, R.X.; Wu, Y.H.; Li, C.Y.; et al. Humidity-controlled dynamic engineering of buckling dimensionality in MoS_2 thin films. *ACS Nano* 2022. [CrossRef]

69. Ren, H.T.; Xiong, Z.X.; Wang, E.Z.; Yuan, Z.Q.; Sun, Y.F.; Zhu, K.L.; Wang, B.L.; Wang, X.W.; Ding, H.Y.; Liu, P.; et al. Watching dynamic self-assembly of web buckles in strained MoS_2 thin films. *ACS Nano* **2019**, *13*, 3106–3116. [CrossRef]

70. Cakir, D.; Sahin, H.; Peeters, F.M. Doping of rhenium disulfide monolayers: A systematic first principles study. *Phys. Chem. Chem. Phys.* **2014**, *16*, 16771–16779. [CrossRef]

71. Luo, M.; Xu, Y.E. Magnetic properties of rhenium disulfide (ReS_2) monolayer doped with different nonmetal atoms. *Optik* **2018**, *158*, 291–296. [CrossRef]

72. Zhou, W.; Zou, X.L.; Najmaei, S.; Liu, Z.; Shi, Y.M.; Kong, J.; Lou, J.; Ajayan, P.M.; Yakobson, B.I.; Idrobo, J.C. Intrinsic structural defects in monolayer molybdenum disulfide. *Nano Lett.* **2013**, *13*, 2615–2622. [CrossRef] [PubMed]

73. Hong, J.H.; Hu, Z.X.; Probert, M.; Li, K.; Lv, D.H.; Yang, X.N.; Gu, L.; Mao, N.N.; Feng, Q.L.; Xie, L.M.; et al. Exploring atomic defects in molybdenum disulphide monolayers. *Nat. Commun.* **2015**, *6*, 6293. [CrossRef] [PubMed]

74. Luo, M.; Shen, Y.H.; Yin, T.L. Structural, electronic, and magnetic properties of transition metal doped ReS_2 monolayer. *JETP. Lett.* **2017**, *105*, 255–259. [CrossRef]

75. Obodo, K.O.; Ouma, C.N.M.; Obodo, J.T.; Braun, M. Influence of transition metal doping on the electronic and optical properties of ReS_2 and $ReSe_2$ monolayers. *Phys. Chem. Chem. Phys.* **2017**, *19*, 19050–19057. [CrossRef]

76. Luo, M.; Xu, Y.E. A first principle study on the magnetic properties of Ag, Al, Li, Mg, and Na doped ReS_2 monolayers. *J. Supercond. Nov. Magn.* **2018**, *31*, 2431–2436. [CrossRef]

77. Li, J.F.; Liao, Z.X.; Xia, B.R.; Wang, T.T.; Gao, D.Q. Tunable ferromagnetic ordering in phosphorus adsorbed ReS_2 nanosheets. *Nanotechnology* **2021**, *32*, 075701. [CrossRef]

78. Zhou, J.; Wu, M.M.; Zhou, X.; Sun, Q. Tuning electronic and magnetic properties of graphene by surface modification. *Appl. Phys. Lett.* **2009**, *95*, 103108. [CrossRef]

79. Zhou, J.; Wang, Q.; Sun, Q.; Jena, P. Electronic and magnetic properties of a BN sheet decorated with hydrogen and fluorine. *Phys. Rev. B* **2010**, *81*, 085442. [CrossRef]

80. Shoda, K.; Kohno, H.; Kobayashi, Y.; Takagi, D.; Takeda, S. Feasibility study for sidewall fluorination of SWCNTs in CF_4 plasma. *J. Appl. Phys.* **2008**, *104*, 113529. [CrossRef]

81. Hong, X.; Cheng, S.H.; Herding, C.; Zhu, J. Colossal negative magnetoresistance in dilute fluorinated graphene. *Phys. Rev. B* **2011**, *83*, 085410. [CrossRef]

82. Hong, X.; Zou, K.; Wang, B.; Cheng, S.H.; Zhu, J. Evidence for spin-flip scattering and local moments in dilute fluorinated graphene. *Phys. Rev. Lett.* **2012**, *108*, 226602. [CrossRef] [PubMed]

83. Nair, R.R.; Sepioni, M.; Tsai, I.L.; Lehtinen, O.; Keinonen, J.; Krasheninnikov, A.V.; Thomson, T.; Geim, A.K. Spin-half paramagnetism in graphene induced by point defects. *Nat. Phys.* **2012**, *8*, 199. [CrossRef]

84. Nair, R.R.; Ren, W.C.; Jalil, R.; Riaz, I.; Kravets, V.G.; Britnell, L.; Blake, P.; Schedin, F.; Mayorov, A.S.; Yuan, S.J.; et al. Fluorographene: A two-dimensional counterpart of teflon. *Small* **2010**, *6*, 2877–2884. [CrossRef] [PubMed]

85. Luo, M.; Shen, Y.H.; Song, Y.X. Structural and magnetic properties of transition-metal adsorbed ReS_2 monolayer. *Jpn. J. Appl. Phys.* **2017**, *56*, 055701. [CrossRef]

86. Yang, S.X.; Wang, C.; Sahin, H.; Chen, H.; Li, Y.; Li, S.S.; Suslu, A.; Peeters, F.M.; Liu, Q.; Li, J.B.; et al. Tuning the optical, magnetic, and electrical properties of $ReSe_2$ by nanoscale strain engineering. *Nano Lett.* **2015**, *15*, 1660–1666. [CrossRef]

87. Tao, P.; Guo, H.; Yang, T.; Zhang, Z. Strain-induced magnetism in MoS_2 monolayer with defects. *J. Appl. Phys.* **2014**, *115*, 054305. [CrossRef]

88. Kan, M.; Wang, J.Y.; Li, X.W.; Zhang, S.H.; Li, Y.W.; Kawazoe, Y.; Sun, Q.; Jena, P. Structures and phase transition of a MoS_2 monolayer. *J. Phys. Chem. C* **2014**, *118*, 1515–1522. [CrossRef]

89. Zhang, Q.; Tan, S.J.; Mendes, R.G.; Sun, Z.T.; Chen, Y.T.; Kong, X.; Xue, Y.H.; Rummeli, M.H.; Wu, X.J.; Chen, S.L.; et al. Extremely weak van der Waals coupling in vertical ReS_2 nanowalls for high-current-density lithium-ion batteries. *Adv. Mater.* **2016**, *28*, 2616–2623. [CrossRef]

90. Xiao, J.; Zhu, H.Y.; Wang, Y.; Feng, W.; Hu, Y.X.; Dasgupta, A.; Han, Y.M.; Wang, Y.; Muller, D.A.; Martin, L.W.; et al. Intrinsic two-dimensional ferroelectricity with dipole locking. *Phys. Rev. Lett.* **2018**, *120*, 227601. [CrossRef]

91. Yu, Y.L.; Jung, G.S.; Liu, C.Z.; Lin, Y.C.; Rouleau, C.M.; Yoon, M.; Eres, G.; Duscher, G.; Xiao, K.; Irle, S.; et al. Strain-induced growth of twisted bilayers during the coalescence of monolayer MoS_2 crystals. *ACS Nano* **2021**, *15*, 4504–4517. [CrossRef] [PubMed]

92. Ma, Z.; Wang, S.; Deng, Q.; Hou, Z.; Zhou, X.; Li, X.; Cui, F.; Si, H.; Zhai, T.; Xu, H. Epitaxial growth of rectangle shape MoS_2 with highly aligned orientation on twofold symmetry a-plane sapphire. *Small* **2020**, *16*, 2000596. [CrossRef]

93. Xu, J.G.; Srolovitz, D.J.; Ho, D. The adatom concentration profile: A paradigm for understanding two-dimensional MoS$_2$ morphological evolution in chemical vapor deposition growth. *ACS Nano* **2021**, *15*, 6839–6848. [CrossRef] [PubMed]

94. Kim, J.; Seung, H.; Kang, D.H.; Kim, J.; Bae, H.; Park, H.; Kang, S.S.; Choi, C.; Choi, B.K.; Kim, J.S.; et al. Wafer-scale production of transition metal dichalcogenides and alloy monolayers by nanocrystal conversion for large-scale ultrathin flexible electronics. *Nano Lett.* **2021**, *21*, 9153–9163. [CrossRef]

95. Aljarb, A.; Fu, J.H.; Hsu, C.C.; Chuu, C.P.; Wan, Y.; Hakami, M.; Naphade, D.R.; Yengel, E.; Lee, C.J.; Brems, S.; et al. Ledge-directed epitaxy of continuously self-aligned single-crystalline nanoribbons of transition metal dichalcogenides. *Nat. Mater.* **2020**, *19*, 1300–1306. [CrossRef] [PubMed]

96. Liao, M.Z.; Wei, Z.; Du, L.J.; Wang, Q.Q.; Tang, J.; Yu, H.; Wu, F.F.; Zhao, J.J.; Xu, X.Z.; Han, B.; et al. Precise control of the interlayer twist angle in large scale MoS$_2$ homostructures. *Nat. Commun.* **2020**, *11*, 2153. [CrossRef] [PubMed]

97. Du, Z.G.; Guo, Y.; Wang, H.Y.; Gu, J.N.; Zhang, Y.Z.; Cheng, Z.J.; Li, B.; Li, S.M.; Yang, S.B. High-throughput production of 1T MoS$_2$ monolayers based on controllable conversion of Mo-based MXenes. *ACS Nano* **2021**, *15*, 19275–19283. [CrossRef] [PubMed]

98. Li, X.F.; Li, B.C.; Lei, J.C.; Bets Ksenia, V.; Sang, X.H.; Okogbue, E.; Liu, Y.; Unocic Raymond, R.; Yakobson Boris, I.; Hone, J.; et al. Nickel particle-enabled width-controlled growth of bilayer molybdenum disulfide nanoribbons. *Sci. Adv.* **2021**, *7*, eabk1892. [CrossRef]

99. Liu, L.; Li, T.T.; Ma, L.; Li, W.S.; Gao, S.; Sun, W.J.; Dong, R.K.; Zou, X.L.; Fan, D.X.; Shao, L.W.; et al. Uniform nucleation and epitaxy of bilayer molybdenum disulfide on sapphire. *Nature* **2022**, *605*, 69–75. [CrossRef]

100. Wu, R.X.; Tao, Q.Y.; Dang, W.Q.; Liu, Y.; Li, B.; Li, J.; Zhao, B.; Zhang, Z.W.; Ma, H.F.; Sun, G.Z.; et al. Waals epitaxial growth of atomically thin 2D metals on dangling-bond-free WSe$_2$ and WS$_2$. *Adv. Funct. Mater.* **2019**, *29*, 1806611. [CrossRef]

101. Wang, J.H.; Xu, X.Z.; Cheng, T.; Gu, L.H.; Qiao, R.X.; Liang, Z.H.; Ding, D.D.; Hong, H.; Zheng, P.M. Dual-coupling-guided epitaxial growth of wafer-scale single-crystal WS$_2$ monolayer on vicinal a-plane sapphire. *Nat. Nanotechnol.* **2021**, *17*, 33–38. [CrossRef] [PubMed]

102. Li, X.B.; Wang, X.; Hong, J.H.; Liu, D.Y.; Feng, Q.L.; Lei, Z.B.; Liu, K.H.; Ding, F.; Xu, H. Nanoassembly growth model for subdomain and grain boundary formation in 1T′ layered ReS$_2$. *Adv. Funct. Mater.* **2019**, *29*, 1906385. [CrossRef]

103. Jing, Q.H.; Zhang, H.; Huang, H.; Fan, X.C.; Zhang, Y.M.; Hou, X.Y.; Xu, Q.Y.; Ni, Z.H.; Qiu, T. Ultrasonic exfoliated ReS$_2$ nanosheets: Fabrication and use as co-catalyst for enhancing photocatalytic efficiency of TiO$_2$ nanoparticles under sunlight. *Nanotechnology* **2019**, *30*, 8. [CrossRef] [PubMed]

104. Wang, X.Q.; Chen, B.; Yan, D.D.; Zhao, X.Y.; Wang, C.L.; Liu, E.Z.; Zhao, N.Q.; He, F. Distorted 1T-ReS$_2$ nanosheets anchored on porous TiO$_2$ nanofibers for highly enhanced photocatalytic hydrogen production. *ACS Appl. Mater. Interfaces* **2019**, *11*, 23144–23151. [CrossRef]

105. Pan, J.; Wang, R.; Xu, X.Y.; Hu, J.G.; Ma, L. Transition metal doping activated basal-plane catalytic activity of two -dimensional 1T′-ReS$_2$ for hydrogen evolution reaction: A first-principles calculation study. *Nanoscale* **2019**, *11*, 10402–10409. [CrossRef]

106. Yang, S.Z.; Gong, Y.J.; Manchanda, P.; Zhang, Y.Y.; Ye, G.L.; Chen, S.M.; Song, L.; Pantelides, S.T.; Ajayan, P.M.; Chisholm, M.F.; et al. Rhenium-doped and stabilized MoS$_2$ atomic layers with basal-plane catalytic activity. *Adv. Mater.* **2018**, *30*, 1803477. [CrossRef]

107. Zhou, Y.; Song, E.H.; Zhou, J.D.; Lin, J.H.; Ma, R.G.; Wang, Y.W.; Qiu, W.J.; Shen, R.X.; Suenaga, K.; Liu, Q.; et al. Auto-optimizing hydrogen evolution catalytic activity of ReS$_2$ through intrinsic charge engineering. *ACS Nano* **2018**, *12*, 4486–4493. [CrossRef]

108. Huang, J.W.; Gao, H.G.; Xia, Y.F.; Sun, Y.H.; Xiong, J.; Li, Y.R.; Cong, S.; Guo, J.; Du, S.Y.; Zou, G.F. Enhanced photoelectrochemical performance of defect-rich ReS$_2$ nanosheets in visible-light assisted hydrogen generation. *Nano Energy* **2018**, *46*, 305–313. [CrossRef]

109. Ng, S.; Iffelsberger, C.; Sofer, Z.; Pumera, M. Tunable room-temperature synthesis of ReS$_2$ bicatalyst on 3D-and 2D-printed electrodes for photo- and electrochemical energy applications. *Adv. Funct. Mater.* **2020**, *30*, 1910193. [CrossRef]

110. Marchiori, E.; Ceccarelli, L.; Rossi, N.; Lorenzelli, L.; Degen, C.L.; Poggio, M. Nanoscale magnetic field imaging for 2D materials. *Nat. Rev. Phys.* **2022**, *4*, 49–60. [CrossRef]

111. Mattiat, H.; Rossi, N.; Gross, B.; Pablo-Navarro, J.; Magén, C.; Badea, R.; Berezovsky, J.; De Teresa, J.M.; Poggio, M. Nanowire magnetic force sensors fabricated by focused-electron-beam-induced deposition. *Phys. Rev. Appl.* **2020**, *13*, 044043. [CrossRef]

112. Vasyukov, D.; Anahory, Y.; Embon, L.; Halbertal, D.; Cuppens, J.; Neeman, L.; Finkler, A.; Segev, Y.; Myasoedov, Y.; Rappaport, M.L.; et al. A scanning superconducting quantum interference device with single electron spin sensitivity. *Nat. Nanotechnol.* **2013**, *8*, 639–644. [CrossRef] [PubMed]

113. Vool, U.; Hamo, A.; Varnavides, G.; Wang, Y.; Zhou, T.X.; Kumar, N.; Dovzhenko, Y.; Qiu, Z.; Garcia, C.A.C.; Pierce, A.T.; et al. Imaging phonon-mediated hydrodynamic flow in WTe$_2$. *Nat. Phys.* **2021**, *17*, 1216–1220. [CrossRef]

114. Ariyaratne, A.; Bluvstein, D.; Myers, B.A.; Jayich, A.C.B. Nanoscale electrical conductivity imaging using a nitrogen-vacancy center in diamond. *Nat. Commun.* **2018**, *9*, 2406. [CrossRef] [PubMed]

115. Wörnle, M.S.; Welter, P.; Giraldo, M.; Lottermoser, T.; Fiebig, M.; Gambardella, P.; Degen, C.L. Coexistence of Bloch and N′eel walls in a collinear antiferromagnet. *Phys. Rev. B* **2021**, *103*, 094426. [CrossRef]

116. Chang, K.; Eichler, A.; Rhensius, J.; Lorenzelli, L.; Degen, C.L. Nanoscale imaging of current density with a single-spin magnetometer. *Nano Lett.* **2017**, *17*, 2367–2373. [CrossRef]